land

MDPI

Article

Quantitative Analysis of Aeolian Sand Provenance: A Comprehensive Analysis in the Otindag Dune Field, Central Inner Mongolia, China

Yingying Cui [1], Yali Zhou [1,*], Ivan Lizaga [2], Zhibao Dong [1,*], Jin Zhang [1], Aimin Liang [3], Ping Lü [1] and Tong Feng [1]

[1] School of Geography and Tourism, Shaanxi Normal University, Xi'an 710062, China; yingyingcui@snnu.edu.cn (Y.C.); hyqi1213@snnu.edu.cn (J.Z.); lvping@snnu.edu.cn (P.L.); 2022304139@snnu.edu.cn (T.F.)
[2] Isotope Bioscience Laboratory—ISOFYS, Department of Green Chemistry and Methods, Ghent University, Coupure Links 653, 9000 Ghent, Belgium; ivan.lizaga@ugent.be
[3] School of Geographical Sciences, Southwest University, Chongqing 400715, China; aimliang@snnu.edu.cn
* Correspondence: ylzhou109@snnu.edu.cn (Y.Z.); zbdong@snnu.edu.cn (Z.D.); Tel.: +86-130-9696-0941 (Y.Z.); +86-139-1946-8009 (Z.D.)

Abstract: The identification and quantification of aeolian sand contributions are essential for understanding the formation of dune fields and mechanisms of modern surface processes. In the present study, we take aeolian sand in the Otindag dune field (hereafter, often referred to as, simply, Otindag) as the research object. The dune field's immediate source is quantitatively identified based on heavy minerals and the Conservativeness Index (CI), Consensus Ranking (CR), and the Consistent Tracer Selection (CTS) method. The primary source area of the aeolian sand was found to be from the northwestern, upwind area of the Otindag (59 ± 14%), followed by the Yinshan Mountain (17 ± 10%) and the lake basin (23 ± 12%). The proposed sediment transport model elucidates that sediments from the upwind of the Otindag are directly transported from the northwest to the Otindag, where they are deposited. Materials from the southern Yinshan Mountains are carried by rivers to the southern edge of the Otindag, where they are subsequently transported by wind and ultimately deposited. The lake deposits within the Otindag also contribute to the aeolian sand supply under the influence of wind. This study demonstrates that the fingerprinting techniques of CI, CR, and CTS serve as successful strategies for conducting quantitative provenance research in dune fields.

Keywords: aeolian sand; heavy mineral; quantitative provenance; Otindag dune field

Citation: Cui, Y.; Zhou, Y.; Lizaga, I.; Dong, Z.; Zhang, J.; Liang, A.; Lü, P.; Feng, T. Quantitative Analysis of Aeolian Sand Provenance: A Comprehensive Analysis in the Otindag Dune Field, Central Inner Mongolia, China. *Land* **2024**, *13*, 1194. https://doi.org/10.3390/land13081194

Academic Editor: Hanoch Lavee

Received: 28 June 2024
Revised: 30 July 2024
Accepted: 31 July 2024
Published: 2 August 2024

1. Introduction

Aeolian sediments, which are widely distributed in arid dune fields areas, are a crucial component of the Earth's surface sediments [1,2]. The expansion and contraction of dune fields play a crucial role in shaping the global climate and environment. This process greatly impacts the atmospheric radiation balance and helps regulate the oceanic carbon cycle [3,4]. Consequently, comprehending the evolution mechanisms of dune fields is important for surface processes and climate change. However, the study of the evolution mechanisms of dune fields is challenging because sand mixes with different sources. Therefore, one of the fundamental tasks is to determine the provenance of aeolian sand sediments from qualitative and quantitative perspectives.

Land desertification is the primary form of environmental degradation in fragile ecological zones, deepening the serious ecological imbalance and leading to a deterioration of the environment, posing a significant threat to human economic development and quality of life [5]. Researchers studying desertification have examined sedimentological characteristics such as grain size, geochemical elements, and minerals in desertification areas to understand the sources and evolution of sandy desertification [6,7]. Knowledge of

the origin of aeolian sand is essential for developing effective models for desertification control. The transition zone between the cropping area and nomadic area is fragile, and strengthening the source and transport mechanism of aeolian sand in this ecotone can provide inspiration for the control of aeolian sand in this ecotone.

The Otindag dune field is located in eastern China, within the semi-arid climate zone, on the edge of the East Asian monsoon region. This area serves as a natural laboratory for studying the formation and evolution of sand dunes in transitional zones between agricultural farming and animal grazing. Since 2000, the Ecological Protection and Construction Project in the Beijing-Tianjin area has achieved remarkable results. The western part of the Otindag still contains large areas of semifixed dunes, which can easily become the source of sandstorms that negatively impact the health of nearby residents. Therefore, studying the provenance of aeolian sand in Otindag not only contributes to understanding the formation mechanism of the dune field but also plays a crucial role in ecological restoration and the well-being of surrounding residents. Several researchers have studied the origin of the sand in this dune field. By analyzing rare earth elements, Liu and Yang proposed that the aeolian sand in the dune field originates from nearby sources rather than distant sources [8]. Xie and Ding analyzed the U-Pb ages and Hf isotopes of detrital zircons from the Otindag since the Last Glacial Maximum and concluded that the primary sources of the dune field are the Central Asian Orogenic Belt (CAOB) and the North China Craton (NCC) [9]. Previous research has indicated that the CAOB and the NCC are the parent source areas of aeolian sand in the Otindag. However, the specific immediate source areas and quantitative contributions have not been determined. It is crucial to determine the immediate source area of aeolian sand in order to effectively implement control measures and ecological restoration in this region.

Provenance tracing can be applied using various methods, such as analyses of heavy minerals, rare earth elements (REEs), Sr-Nd isotopes and quartz oxygen isotope, and detrital zircon U-Pb dating [10–14]. Among them, heavy minerals have emerged as a classic technique for provenance tracing owing to their resistance to transportation abrasion, strong stability, and ability to retain source rock information effectively [15,16]. Rock combinations in the source area and the regional structural background can be characterized by combining common heavy minerals [17–19]. However, the traditional method of identifying heavy minerals under the microscope is a manual process that is time-consuming, labor-intensive and requires a high level of professional expertise. Moreover, there is a possibility of systematic errors when different operators are involved. Nevertheless, with scientific and technological advancements, the Quantitative Evaluation of Minerals by scanning electron microscopy (QEMSCAN) has been developed, offering a solution to this problem. It automates the identification of mineral types and provides a significant amount of data, thereby enhancing the accuracy of heavy mineral identification.

In order to determine different source contributions, fingerprinting methods have been proposed since the early 1980s as a means of provenance tracing [20]. The procedure estimates the relative contribution of each potential source, using a variety of selected tracer properties. Initial studies were performed based on a single tracer [21]. However, the inclusion of quantitative mixing models and the use of multiple tracers enabled researchers to discriminate more than two sources [22,23]. Nowadays, numerous studies use fingerprinting techniques to examine specific catchment management problems [24,25], and to evaluate processes [26] and contamination in the river and coastal waters [27,28]. In recent times, the technique has gained popularity regarding the understanding of aeolian sand provenance in desert environments [29–31]. The crucial steps to implement the technique involve the selection of conservative tracers for differentiating potential sources. Lizaga discussed the main methods of tracer selection and found that when traditional approaches such as the mixing polygon or three-step method (i.e., the range test, the Kruskal-Wallis test, and the discriminant function analysis test) are used for selecting tracers, erroneous tracers could be included while informative tracers removed, leading to errors in both Frequentist and Bayesian models [32,33]. In this regard, the Conservativeness Index (CI),

Consensus Ranking (CR), and Consistent Tracer Selection (CTS) methods offer crucial information on the relationship between sources and mixtures and are applied before unmixing as they are model-independent. These methods also facilitate the detection of non-consensual and non-consistent tracers, as well as the extraction of multiple partial solutions from a dataset.

Following the mentioned state-of-the-art methods, the present study aimed to achieve a comprehensive understanding of the aeolian sand sources of the Otindag, quantify the contribution of each source to the dune field, and elucidate the supply mechanisms of sediments in the dune field. For this purpose, heavy mineral data was applied as tracers to quantify the contributions of each potential source area to the dune field aeolian sand.

2. Materials and Methods

2.1. Study Area

The Otindag dune field is located in the Xilin Gol League in the central part of the Inner Mongolia Autonomous Region (41.93–44.40° N, 112.37–117.95° E). It lies within the Erenhot Basin, bordered by the Greater Khingan Range to the east and the Yinshan Mountains to the south (Figure 1a,b). The area falls within the temperate monsoon semi-arid climate zone, with an average annual temperature of 0 to 3 °C and an annual precipitation ranging from approximately 200 to 400 mm. The precipitation increases from northwest to southeast. The Otindag primarily consists of Tertiary and Quaternary sediments. Based on the sediments and wind regimes, the Otindag can be divided into three major areas. The first area is the upwind area, located in the western part of the Otindag. Here, the exposed sediments primarily consist of red clay layers, along with interbedded sediments of red-brown fluvial and lacustrine gravel (Figure 2g). Additionally, river-lake facies sediments of green-gray and turbid yellow colors, as well as gravelly Gobi sediments, are present (Figure 2c,f). These sediments originate from the surrounding orogenic belt areas that were transported through fluvial and aeolian processes during the geological history [34]. The second area forms the main body of the Otindag, with a wide distribution of aeolian sand sediments and a small amount of fluvial and lacustrine sediments since the late Pleistocene. The western part of the Otindag is mainly composed of semi-fixed sand dunes, with barchan dunes and chain dunes (Figure 2b). The eastern part of the dune field is mainly composed of fixed sand dunes. Influenced by the prevailing wind direction within the Otindag, the sand dunes are roughly arranged in a northwest-southeast direction. The northern edge of the dune field connects with the Abaga lava platform. The sedimentary sequence of the local basalt lava platform includes basalt, baked layer, aeolian sand, multi-layered gray-green fluvial and lacustrine facies, and tertiary red clay deposits (Figure 2d,e). The third area, located in the southeast downwind direction of the Otindag, is the loess accumulation area. It is mainly distributed in the mountains, hills, and basins on the eastern and southern edges of the Otindag. The quaternary sediments in this area mainly consist of ancient aeolian sand, dune field paleosol, sand loess, and loess.

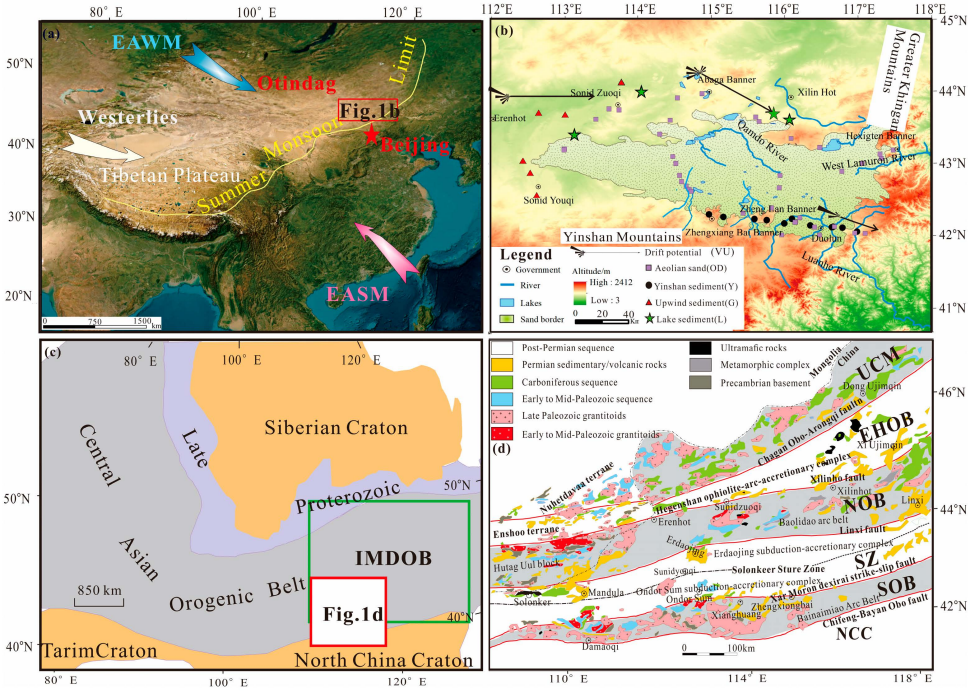

Figure 1. (**a**) Atmospheric circulation pattern of China including the study region. (**b**) Locations of the Otindag and sampling points. The sand drift potential was calculated using wind data from the US Meteorological Data Center (https://www.ncei.noaa.gov/maps/hourly/ (accessed on 16 December 2023)) following the method of Fryberger and Dean [35]). (**c**) Structural framework of Central Asian Orogenic Belt including the study region (modified after Wang Zhigang [36]). (**d**) Schematic map of the geological characteristics of the Otindag and its surrounding areas, with modifications based on previous studies [36,37]. Abbreviations: SOB, the southern orogenic belt; SZ, the Solonker suture zone; NOB, the northern orogenic belt; EHOB, the Erenhot–Hegenshan ophiolite belt; UCM, the Uliastai continental margin; NCC: North China Craton; IMDOB: Mongolia–Daxing'an Orogenic Belt.

The Otindag falls within the IMDOB (Figure 1c), which is a part of the CAOB. Geologically, it is separated from the NCC by the Chifeng-Bayan Obe fault in the southern region (Figure 1d). The dune field includes several fault zones from north to south, including the Xilinhot fault, Linxi fault, Xar Moron dextral strike-slip fault, and Chifeng-Bayan Obe fault [38]. These fault zones divide the Otindag into three smaller structural units: the NOB, the SZ, and the SOB (Figure 1d). The NOB, which records Early to Middle Paleozoic subduction–accretion processes of the Paleo-Asian Ocean, comprises several accretionary and metamorphic complexes, with intermittent exposures of metamorphic rock formations in the Sonidzuoqi-Xilinhot granite-metamorphic rock belt [39]. The Darinor volcano group and the Abaga volcano group expose multi-level lava platforms. The Paleo-Asian Ocean is believed to have finally closed at the SZ, which records the terminal evolution of the Paleo-Asian Ocean in the southeastern CAOB [36]. The SZ is characterized by sporadic distributions of mélanges and remnants of arcs and ophiolites, with ages ranging from the Early Permian to the Early Triassic [40]. The SOB comprises Paleozoic blueschists, a series of ophiolite fragments, arc-like magmatism, and volcano-sedimentary sequences [38].

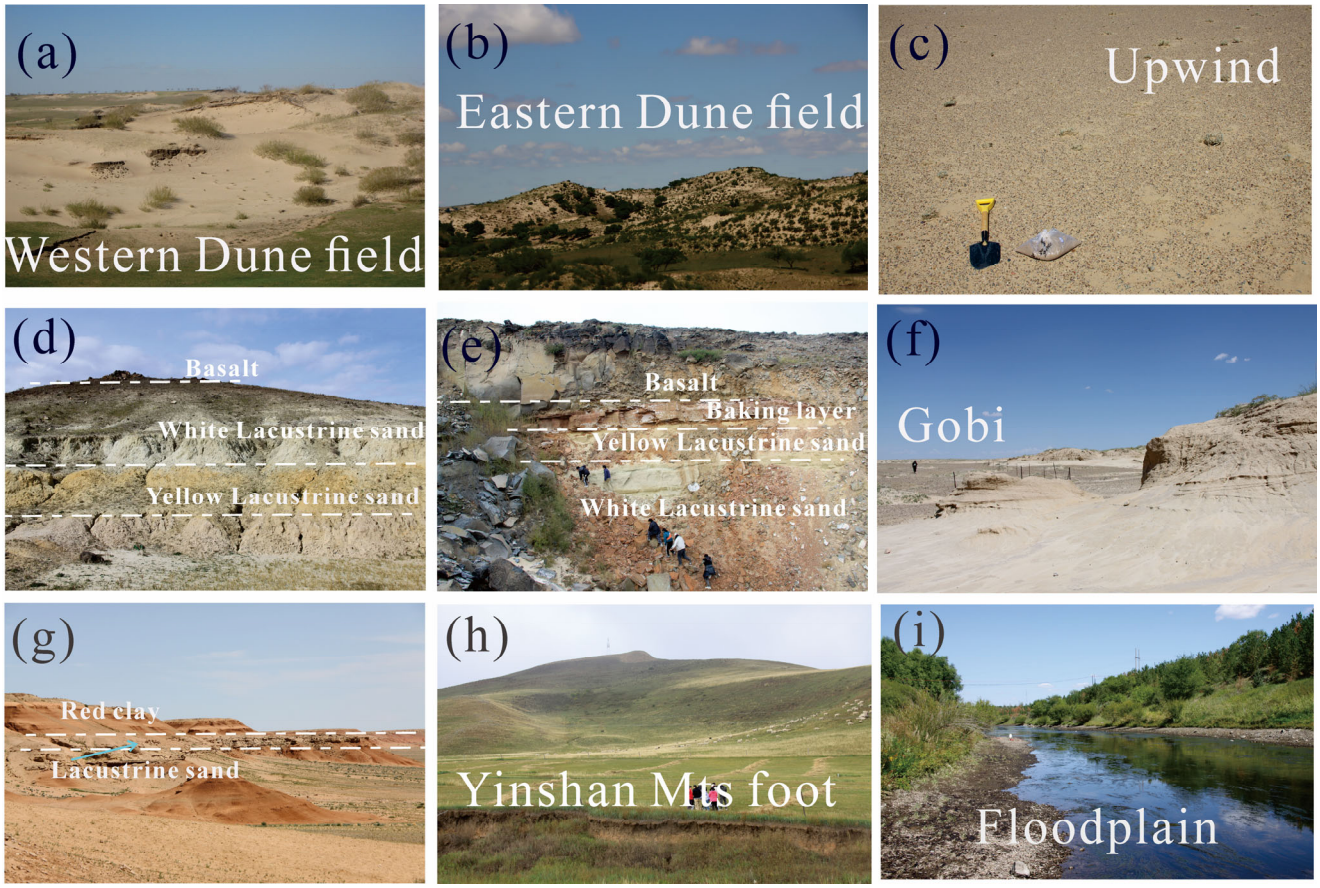

Figure 2. Photos of representative land surface in the Otindag and the potential sources. (**a**) The eastern area of Otindag dune field. (**b**) The western area of Otindag Dune field. (**c**) Mixed surface sediments from upwind erosion areas on Otindag. (**d**,**e**) Palaeo-lacustrine facies sediments under basalt. (**f**) The gobi located the upwind. (**g**) Palaeo-lacustrine sand eroded by wind. (**h**) The northern foot of Yinshan Mountain. (**i**) The floodplain of the Luanhe River.

The wind in the Otindag is predominantly strong, with prevailing west and northwest directions. The average annual wind speed is 3.5 m/s, with maximum speeds reaching 24–28 m/s. There are approximately 50–70 windy days per year. In this study, wind regime data from Abaga, Duolun, and Erenhot spanning from 2017 to 2022 were used to evaluate the sand drift potential at these three locations. Specifically, five key wind-related parameters were calculated (Table 1), including the drift potential (DP), resultant drift potential (RDP), resultant drift direction (RDD), and directional variability (RDP/DP). Abaga Banner, located on the northern edge of the dune field, exhibits an RDP of 306.66 (VU), with the RDD from northwest to southeast. Erenhot is located on the western edge of the dune field with RDP of 279.41 (VU) and RDD from west to east. Duolun, located on the southeastern edge of the dune field, has an RDP of 93.63 (VU) and RDD from northwest to southeast (Table 1, Figure 1b). Based on Fryberger and Dean's classification of wind regimes, sediment transport in Abaga Banner and Erenhot occurred under high-energy wind environments, whereas that in Duolun occurred under a low-energy wind environment. Overall, the Otindag dune field is characterized by an intermediate-high energy wind environment, with the main drift direction being from northwest to southeast.

Table 1. Results of drift potential at meteorological stations around the Otindag.

Station	DP (VU)	RDP (VU)	RDP/DP	RDD (°)	PWD	Wind Energy Environment
Abaga	711.92	306.66	0.43	118.09	WN	High
Erenhot	393.54	279.41	0.71	269.82	W	High
Duolun	100.46	93.63	0.93	109.42	WN	Low

Note: DP (VU), drift potential; RDP (VU), resultant drift potential; RDP/DP, directional variability; RDD (°), resultant drift direction; PWD, prevailing wind direction; "VU", the vector unit of sediment transport potential (DP) and composite sediment transport potential (RDP).

2.2. Sampling

Through field investigation, modern aeolian sand was found to be widely distributed throughout the Otindag. A total of 39 surface aeolian sand samples (abbreviated as OD) were collected from dunes and interdune areas (Figure 1b). Three other types of samples were collected from three major potential source areas that were determined by fluvial-aeolian system directions. The first type was collected from the upwind potential provenance area in the northwest: 2 gray-yellow Gobi samples (Figure 2f) and 4 samples of gray-yellow surface sand mixed with gravel (Figure 2c), abbreviated as G (Figure 1b). The second type of sediment samples was collected from the southern source area, representing sediment transport by rivers: 7 alluvial deposit samples from the northern foot of the Yinshan Mountains (Figure 2h) and 4 samples from the floodplains of the Luanhe River (Figure 2i), collectively referred to as sediments from the northern foot of the Yinshan Mountains, abbreviated as Y (Figure 1b). The third category consists of Paleo-lacustrine sediments that are distributed on the edge of Otindag. Specifically, 7 samples were collected from ancient lacustrine sand layers found under the basalt strata (Figure 2d,e), and 1 sample from wind-eroded ancient lacustrine sand sediments (Figure 2g), collectively referred to as lake sediments, abbreviated as L (Figure 1b). The age of the lacustrine sand layers under basalt pressure that we collected is roughly in the Pliocene, predating the modern surface sand layers. This suggests that he could provide sand for the modern surface.

2.3. QEMSCAN Method for Heavy Minerals Analyses

QEMSCAN is based on Scanning Electron Microscopy (SEM) and is linked with energy dispersive spectrometry, allowing very rapid, automated, and quantitative mineralogical analysis. The QEMSCAN method offers rapid identification of multiple mineral particles and counting of a larger number of particles per sample compared to traditional optical heavy mineral counting analysis. The latter method is slow and typically features a count of fewer than 1000 particles per sample. Originally developed to support the mining industry, the QEMSCAN method is now also used in sedimentology [41–43]. The Mineral Dissociation Analyzer 650F (MLA650F) manufactured by the Czech company FEI is combined with the FEI SEM and the XFlash-6130 energy-dispersive X-ray spectrometer (EDS) manufactured by Bruker. This instrument can automatically identify 10,000 mineral particles within 1 h. The specific experimental process is shown in Figure 3.

After the samples were evenly divided, approximately 2 g of each sample was directly embedded with resin, polished, and carbonized to prepare the target, and mineral analysis was performed using MLA650F. The experiment was conducted with the voltage under the high vacuum mode: 25 KV, scan speed (step length) of 16, and working distance of 13 mm. The minimum particle size of the test particle was 20 pixels, which is approximately equal to 5 μm, and the number of test particles was at least 10,000. Finally, data from more than 10,000 mineral particles were processed, and commonly used mineral grains were calculated.

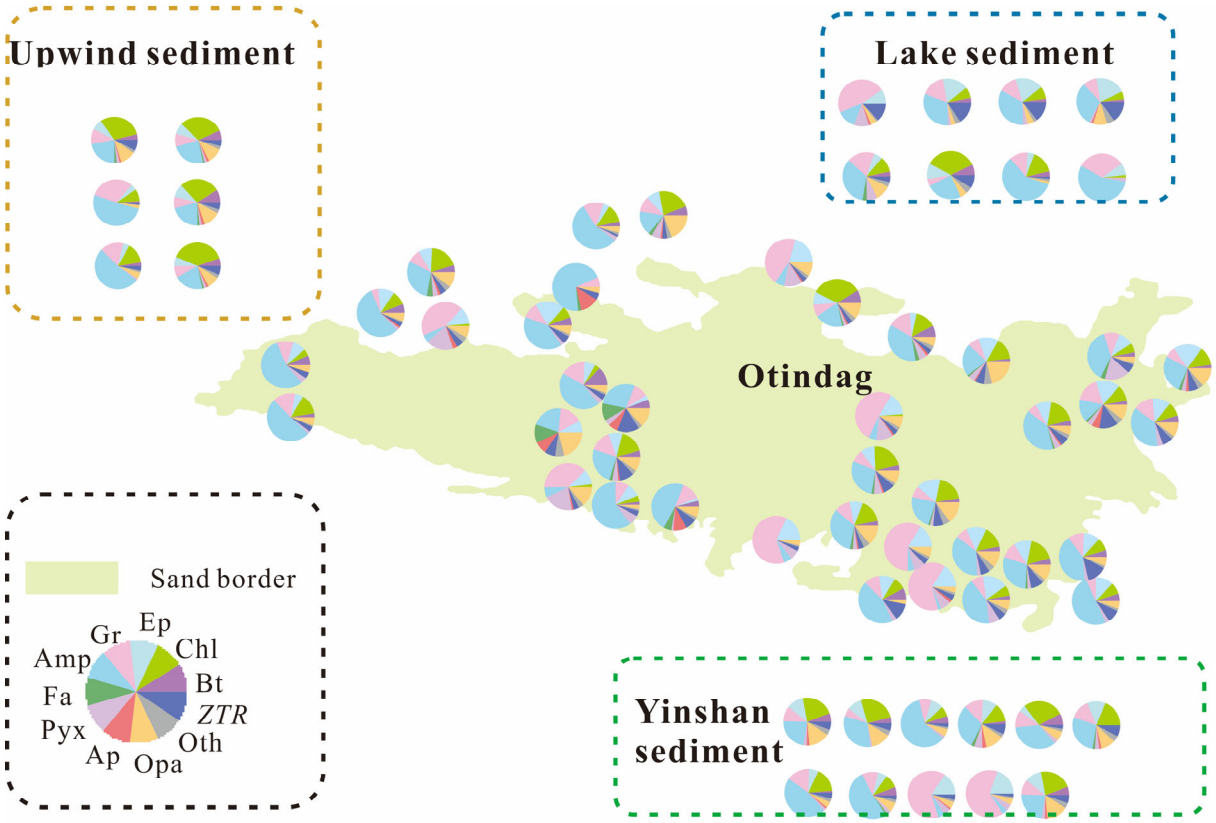

Figure 3. The fan chart of heavy mineral content of all samples from the Otindag and its potential source area. Amp: Hornblende + actinolite + tremolite, Gr: andradite + spessartite + almandine + pyrope, Ep: Epidote + Zoisite + Allanite, Chl: Chlorite, Bt: biotite, ZTR: zircon + tourmaline + rutile, Oth: monazite + spinel + Sphene, Opa: ilmenite + magnetite + goethite, Ap: apatite, Pyx: orthopyroxene + clinopyroxene, Fa: fayalite.

2.4. Heavy Mineral and Rock Indexes

Determining whether sediments have been affected by hydraulic sorting and diagenetic dissolution is a prerequisite for heavy mineral analysis, primarily based on the combination of the following six parameters as criteria: The "Heavy Mineral Concentration index" (Counting-HMC), "Transparent Heavy Mineral Concentration index" (Counting-tHMC), "Source Rock Density index" (Counting-SRD), "Transparent Heavy Mineral Density index" (Counting-ΔtHM), %OP and %ZR [44]. The calculation formula is as follows

$$\text{Counting} - \text{HMC} = \frac{\text{Number of heavy mineral grains}}{\text{Number of total grains} - \text{Unknown} - \text{No XRay} - \text{Low Counts}} \times 100$$

$$\text{Counting} - \text{tHMC} = \frac{\text{Number of transparent heavy mineral grains}}{\text{Number of total grains} - \text{Unknown} - \text{No XRay} - \text{Low Counts}} \times 100$$

$$\text{Counting} - \text{SRD} = \frac{2.65 \times \text{nL} + 5 \times \text{nO} + \delta 1 \times \text{nT1} + \delta 2 \times \text{nT2} + \delta 3 \times \text{nT3} + \cdots}{\text{Number of total grains} - \text{Unknown} - \text{No XRay} - \text{Low Counts}}$$

$$\text{Counting} - \Delta\text{tHM} = \frac{\delta 1 \times \text{nT1} + \delta 2 \times \text{nT2} + \delta 3 \times \text{nT3} + \ldots}{\text{Number of total transparent mineral grains}}$$

where nL is the number of light mineral grains, nO is the number of opaque heavy mineral grains, δ1 is the density of one species of transparent mineral, and nT1 is the number of grains of that species of mineral.

$$\%\text{OP} = 100 \times \text{Opaque heavy minerals}/\text{total heavy minerals})$$

$$\%\text{ZR} = 100 \times (\text{Zircon} + \text{Rutile})/(\text{Zircon} + \text{Tourmaline} + \text{Rutile}))$$

Heavy mineral-related indicators such as ATi (ATi = 100 × Apatite/(Apatite + Tourmaline)), GZi (GZi = 100 × Garnet/(Garnet + Zircon)), POS (POS = 100 × (Pyroxene + olivine + spinel)/Transparent heavy mineral), MZi (MZi = 100 × Monazite/(Monazite + Zircon)), and ZTR (ZTR = 100 × (Zircon + Tourmaline + Rutile)/Transparent heavy mineral), are also commonly used to assist provenance analysis [16,45,46].

2.5. Quantitative Provenance Analysis

To identify the optimal sets of tracers, we utilized the CI, CR, and CTS methods. To identify the optimal sets of tracers, we utilized the Conservativeness Index (CI), Consensus Ranking (CR), and Consistent Tracer Selection (CTS) methods. CI is a non-parametric test, similar to a more sophisticated version of the range test [47]. CR is a scoring function based on several random debates between tracers. Higher CI and CR scores indicate higher consensus and conservative behavior [32]. CTS identifies the most discriminant tracers similar to the DFA. In addition, CTS also takes into account the mathematical properties of the model, such as 3 sources must have 3 or more tracers to ensure consistency in over-determined datasets [33]. A more detailed description of the methods and principles can be found in the Supplementary Materials.

In combination with the cited methods included in the user-friendly R package FingerPro [48,49], the state-of-the-art unmixing model of the package was applied to estimate the different sediment source contributions for all the samples and their multiple consistent solutions. In this study, the measured minerals and mineral parameters of the three potential source areas were input to the model along with the mineral and mineral parameters of a single dune field aeolian sand sample. In the initial step, tracers meeting CR > 85 and CI > 15 conditions were retained, which were considered to be conservative and stable. In the next step, those tracers were selected for the CTS analysis. In this step, the multiple solutions extracted from the CTS were evaluated prioritizing the ones corresponding to the most discriminant solutions. The main advantage of the CTS becomes evident in this step. Unlike other methods, the CTS reveals different consistent solutions, avoiding the concealment of valuable information by allowing the model to make decisions. This flexibility enables us to leverage expert knowledge when needed, providing insights into the origin of multiple solutions. Subsequently, the selected tracers were unmixed. In the third step, the convergence of the multiple unmixed results to common or multiple solutions was evaluated. In a word, CR, CI, and CTS are a step-by-step relationship, and we select the most suitable tracer through these three processes for the final quantitative analysis. Detailed information about the methodology and model used can be found in the original research [32,33,49] and the R4.4.3 code is available online at https://github.com/eead-csic-eesa/fingerPro (accessed on 16 March 2024).

2.6. Multidimensional Scaling

Multidimensional Scaling (MDS) algorithm is a data reduction and visualization method. It can be used to observe and analyze data intuitively while maintaining the distance relationship between data points. The core idea of the MDS algorithm is to use a distance matrix to represent the similarity or correlation between data points. This method has the advantage that it is relatively easy to calculate and does not need to provide prior knowledge. This method is widely applied to heavy mineral data by using the similarity between the data for compositional analysis [44]. The MDS is implemented in the "Provenance" package [50] in the R Studio. "Provenance4.3" is a software package in the R programming environment, which aims to facilitate the visualization and interpretation of 'Big Data' in the context of sedimentary provenance analysis. After installing R from http://r-project.org (accessed on 30 March 2024), provenance can be installed by typing.

3. Results

3.1. Heavy Mineral Composition

The heavy mineral composition of aeolian sand and its potential source areas in the Otindag are shown in Table S1. A total of 21 heavy minerals were measured in Otindag. The heavy mineral composition of the Otindag aeolian sand was dominated by Hornblende, chlorite, and garnet, which accounted for 27%, 9%, and 18% respectively. The contents of Pyroxene, Actinolite, Epidote, and Goethite are relatively high, each exceeding 4%. The content of extremely stable heavy minerals such as zircon, rutile, and tourmaline was low. The heavy mineral assemblage of aeolian sand suggests that the source area contains acidic igneous rocks, medium and low-grade metamorphic rocks, and medium-basic igneous rocks. In addition, the same mineral showed wide variation across different areas of the Otindag, indicating multiple source areas.

The major heavy mineral assemblage in the three potential source areas is similar to that of Otindag eolian sand, which is hornblende + chlorite + garnet (Figure 3). However, the main mineral content varied (Table S1). Upwind sediments contained more chlorite 25%, lake sediments had higher amounts of epidote (8%) and tourmaline (5%), and Yinshan mountain sediments had higher amounts of garnet (21%).

Figure 3 reveals spatial differences in the heavy mineral content of Otindag samples. The western and northwestern parts of the Otindag have higher contents of amphibole and chlorite, closely resembling the mineral composition of the upwind erosion areas. The southern part of the Otindag has higher contents of amphibole, garnet, and chlorite, with the high garnet content likely related to sediment from the Yinshan Mountains. The northeastern part of the Otindag shows higher contents of amphibole, epidote, and chlorite, with the higher epidote content possibly originating from lacustrine deposits. The spatial variations in heavy mineral assemblages across the Otindag indicate multiple source areas for the Otindag aeolian sand.

3.2. Unmixing of the Sand Source Contributions

One of our main goals was to quantify the source of eolian sand in Otindag. In order to achieve this goal, we use the measured mineral data and effective mineral indicators as tracers and select the most conservative, consensual and consistent tracers by the use of the CI, CR, and CTS methods to estimate the contribution of different source regions. Figure S1 (all triangles) shows a ternary plot of all possible predictions of the contribution of each mineral and mineral parameter to the aeolian sand in sample OD-1. The results of the CI and CR techniques (Figure S1) enable the identification of minerals and rock indexes that effectively characterize potential source areas as conservative tracers. In the OD-1 sample, Sps, Zo, Gt, Ep, Bt, Ap, ΔtHM (Counting-ΔtHM), Rt, Chl, SRD (Counting-SRD) are con-servative tracers because they have physical solutions (i.e., solutions are inside the physi-cal space defined by the ternary diagrams) and they have higher CR and CI values than most of the other tracers.

Besides selecting tracers with high CI and CR values, it is still possible to have multiple consistent solutions in a dataset. Therefore, the CTS method is used to rank the possi-ble consistent solutions according to their discriminant ability (Dmax) [33]. In the OD-1 sample (Table 2), the six most discriminant, consistent, and conservative pairs of tracers were screened by the CTS method, with the first pair composed by Zo and Gt was the most discriminant. It is worth noting that the model can obtain multiple solutions due to differ-ences in the final input tracer, and if most of the multiple solutions point to similar out-comes, it indicates that the optimal solution exists. For example, as visible in Table 2 we observe that the first, second, fourth, and sixth pairs of tracers point to the same solution (approx. 0.11%, 0.16%, 0.73%), while the third and fifth point towards a different solution (approx. 0.02%, 0.52%, 0.46%). Therefore, among the two main solutions of OD-1, we choose the one with higher discriminant capacity and consistency as the final pair. After this step, by following the CTS method, we include the tracers under a normalized error threshold $\varepsilon = 0.05$ regarding the selected pair to obtain the final tracer selection that will

be used as input in the model. Similarly to OD-1, other aeolian sand samples were also pro-cessed, and their final quantitative results were obtained using the same procedure (code available at github.com/eead-csic-eesa/fingerPro) (accessed on 16 March 2024).

Table 2. The first six minimal compatible and conservative tracer sets (formed by pairs in the case of three sources) were extracted from the Mix-sample OD-1. The pairs are ordered based on the discriminant capacity (Dmax), with 'cons' representing the mathematical consistency of each pair.

id	w1	w2	w3	Dw1	Dw2	Dw3	cons	Dmax
Zo Gt	0.11	0.16	0.73	0.26	0.31	0.24	0.44	0.31
Sps Gt	0.16	0.15	0.69	0.29	0.31	0.32	0.46	0.32
Ep Sps	0.02	0.52	0.46	0.32	0.36	0.34	0.45	0.36
Zo Ap	0.14	0.09	0.77	0.30	0.38	0.30	0.39	0.38
Zo Ru	−0.05	0.46	0.59	0.34	0.41	0.38	0.37	0.41
Ap Sps	0.19	0.08	0.73	0.30	0.42	0.35	0.42	0.42

As shown in Figure 4, the average GOF of aeolian sand in the dune field is 98 ± 0%. The northwest upwind area of the dune field appeared as the dominant source, accounting for 59 ± 14% of the total amount on average. The Yinshan Mountain sediments and Lake sediments contributed 17 ± 10% and 23 ± 12%, respectively.

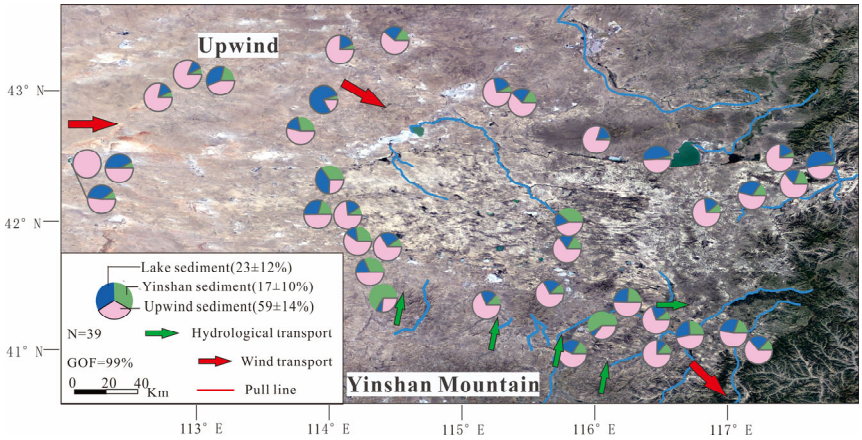

Figure 4. Spatial pattern of provenance contributions of each source type to the Otindag. GOF, goodness of fit; N, sample number. Sediment wind transport potential (red arrow), hydrodynamic transport (green arrow).

4. Discussion

4.1. Influencing Factors of Heavy Mineral Tracing

When using features such as sediment-heavy mineral assemblages to trace the provenance of sediments, it is necessary to first determine whether the mineral composition of the sediments is affected by hydraulic sorting or diagenetic dissolution. Hydraulic sorting will cause heavy minerals in homologous sediments to deviate in different grain size ranges and under different hydrodynamic environments. Diagenetic dissolution will enrich stable heavy minerals. These are important factors that need to be considered in provenance analysis. This study mainly adopted the method proposed by Zhang [44] to reduce the impact of hydraulic sorting or diagenetic dissolution.

For all the collected samples, the Counting-HMC values ranged from 4 to 51, the Counting-tHMC values ranged from 4 to 51 (Table S2), and both values were greater than 1. This suggests a weaker influence of diagenetic dissolution on the sediments in the study area [45]. If the mineral composition of sediments is affected by hydraulic sorting, the Counting-SRD value will be larger, even greater than approximately 3.5. The counting-SRD of the study area was around 2.7, indicating a weak influence of hydraulic sorting. If

indicators such as %OP and %ZR that reflect hydraulic sorting show an obvious positive correlation with indicators such as Counting-ΔtHM, the study area is subject to hydraulic sorting. Linear fitting of Counting-ΔtHM and indices such as %OP and %ZR for the samples (Figure 5) revealed no distinct correlation between the two sets of data, with goodness-of-fit R^2 values of 0.0722 and 0.0388, respectively. The above evidence shows that hydraulic sorting or diagenesis has relatively weak influences on the mineral assemblage of the Otindag and its potential source areas. In other words, the heavy mineral assemblage information of the Otindag and its surrounding sediments can reflect the provenance information.

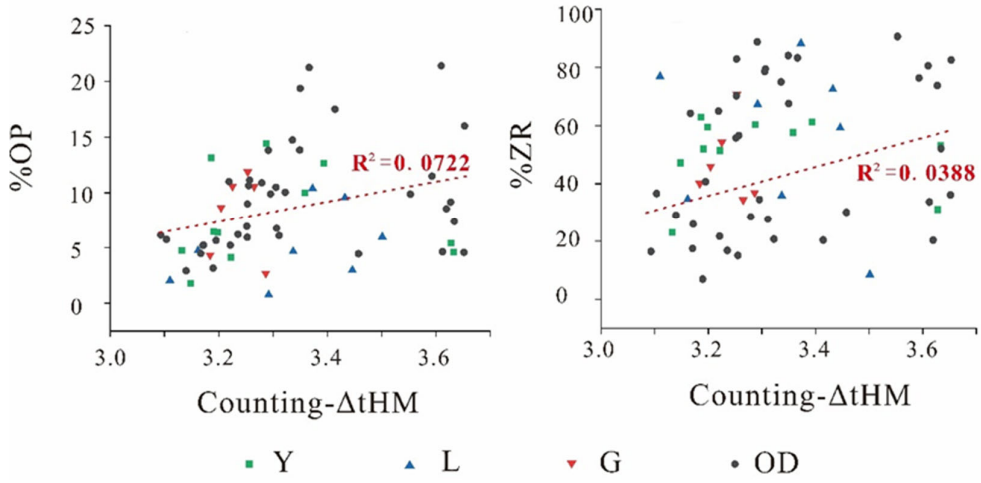

Figure 5. Otindag dune field aeolian sands (OD), upwind sediments (G), lake sediments (L), and Yinshan sediments (Y) correlation analysis of Counting-ΔtHM and %OP and Counting-ΔtHM and %ZR.

4.2. Spatial Heterogeneity of Aeolian Sand Sources

Comparative analysis of the main heavy mineral assemblages is one of the traditional methods used to diagnose the rock types in sediment source areas. The overall content of hornblende and chlorite in the Otindag is relatively high, primarily derived from the medium-acidic granite and greenschist in the northwestern upwind area. In the southern part of Otindag, the content of garnet and Opaque minerals is higher, mainly sourced from the metamorphosed intermediate-basic rocks of the Yinshan Mountains. In the northeastern part of Otindag, the content of augite is also relatively high, primarily originating from ancient lacustrine deposits underlain by basalt.

In order to separate provenance information from heavy mineral assemblage information, Morton and Hallsworth [19] proposed the relative content of mineral pairs with similar hydrodynamic properties and stable chemical properties as an index for identifying actual changes in provenance characteristics. Mineral pairs are categorized into apatite and tourmaline (ATi), garnet and zircon (GZi), and monazite and zircon (MZi) based on their hydrodynamic sorting conditions. These minerals have similar densities and remain relatively stable even during deep burial.

In arid and semi-arid environments, ATi reflects the mineral composition of the source area. The study area has an arid or semi-arid climate, and the high ATi value suggests that acidic igneous parent rocks contribute [51,52]. The rang ATi of the Otindag is from 3 to 86 (mostly >20) and ATi values are higher in the north than in the south (Figure 6c). It indicates the significant influence of granite on the Otindag and the northern part of Otindag is most affected by late Paleozoic granite (Figure 1b). The relative content of GZi can reflect the degree of influence of the metamorphic rocks on the sample. In the current study, the GZi index of modern aeolian sand in the Otindag was found to be 74 to 100, indicating that the provenances in the study area are strongly affected by the metamorphic rocks (Figure 6a), such as the Wendur Group, Baoyintu Group and the Xilingol Complex in the northern part of the study area [53]. The MZi index of modern aeolian sand in the Otindag was found to be 2 to 31 and the highest value was distributed in the southern part of Otindag

(Figure 6d). The POS can reflect the contribution of basic rocks and ultrabasic rocks in the source area [16]. The average POS index of aeolian sand in the Otindag dune field was 6%, with a wide variation range of 1 to 23% (mostly <8), reflecting the low contribution of basic rocks to the Otindag. The high-value distribution of POS is concentrated in the vicinity of basic basalt (Figure 6b).

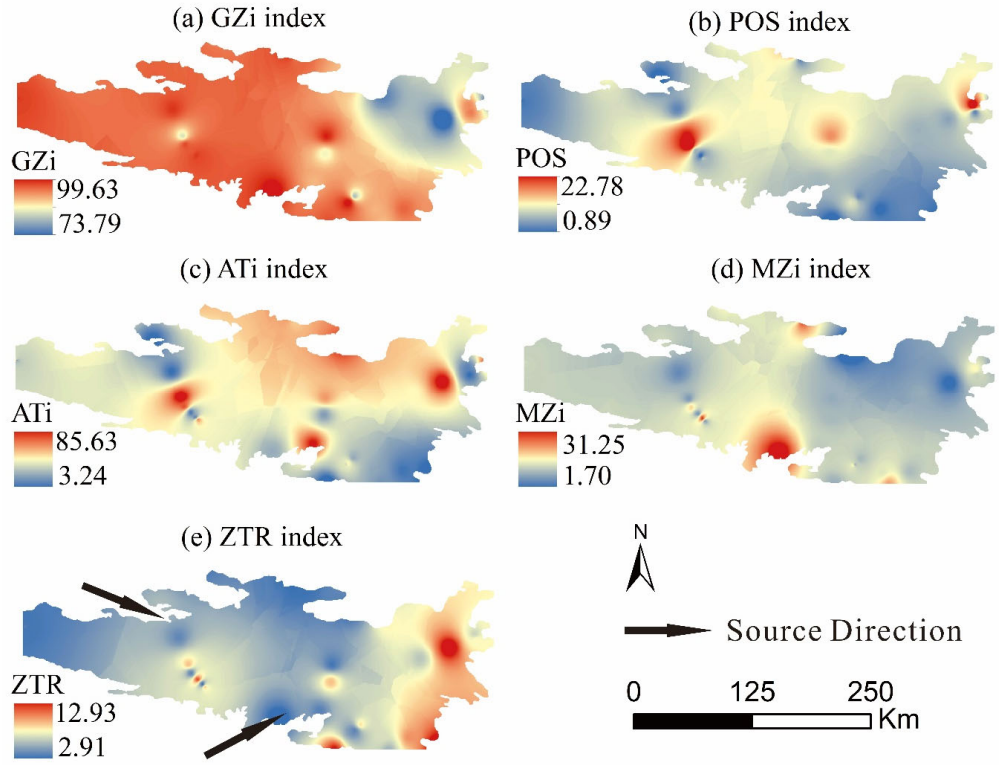

Figure 6. The spatial heterogeneity of provenance in Otindag was determined by the Kriging spatial interpolation diagram of the GZi index (**a**), POS index (**b**), ATi index (**c**), MZi index (**d**), and ZTR index (**e**).

On the whole, the Otindag is primarily affected by acidic igneous rocks and metamorphic rocks, with a small influence from basic volcanic rock fragments. ATi, GZi, POS, and MZi all exhibited large variation ranges, which suggests the spatial heterogeneity of provenance in Otindag was determined.

Hubert [46] proposed the application of the content of highly stable minerals such as zircon, tourmaline, and rutile (ZTR) in sediments to assess sediment maturity. ZTR can serve as an indicator of sediment transport distance to some extent. A higher ZTR value suggests a greater transport distance. As depicted in Figure 6e, the ZTR value of the Otindag increases from northwest to southeast, indicating that the modern surface aeolian sand primarily originates from the upwind area of the Otindag through transport by northwest winds. Furthermore, the lower ZTR value in the south of the dune field suggests that modern aeolian sand in the southern Otindag region originates from the Yinshan Mountains.

The ternary plots of mineral indexes ATi, POS, and MZi (Figure 7a) show that the aeolian sand in the Otindag overlaps with upwind sediments and sediments from the Yinshan Mountains, all characterized by high ATi values. The ternary plot of the main heavy mineral assemblage (Figure 7b) indicates that all three potential source areas of the aeolian sand in the Otindag overlap, and all contain high contents of amphibole, chlorite, and garnet. The MDS (Figure 7c) plot indicates that the aeolian sand in the Otindag has the strongest correlation with the sediments from the upwind areas, with the Yinshan and lake sediments following. In summary, while the aeolian sand in the Otindag shows some similarity to

sediments from all three potential source areas, it has the strongest similarity to the upwind sediments, which may suggest that the upwind area is the primary source area.

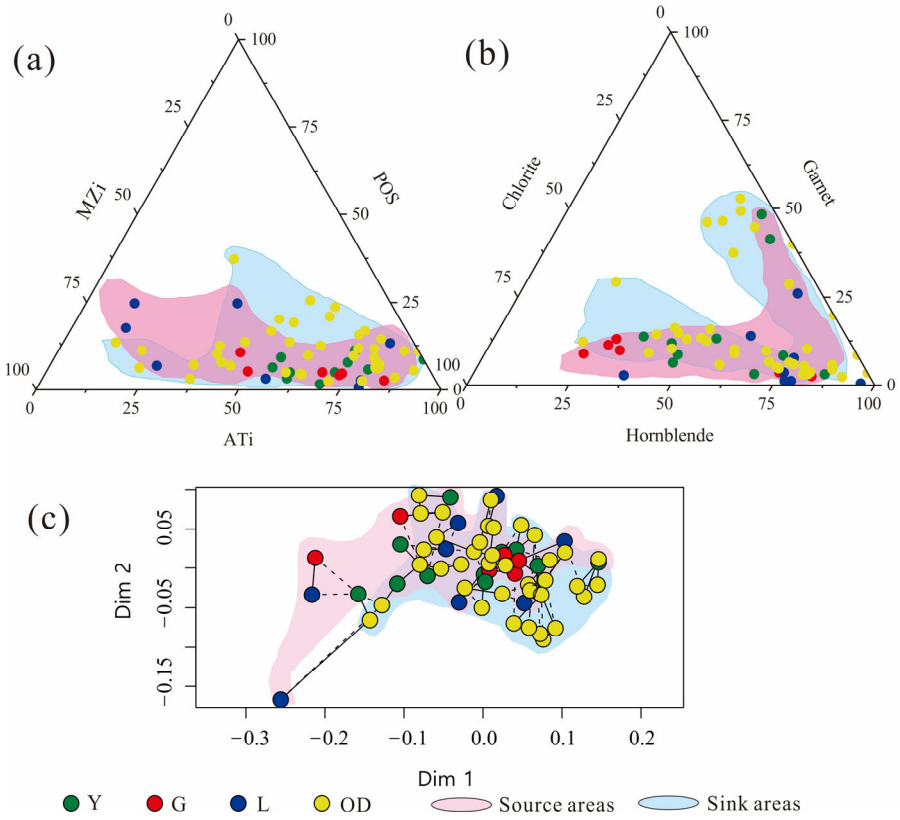

Figure 7. (**a**,**b**) The ternary diagrams of heavy mineral and heavy mineral index of the aeolian sands from the Otindag and its potential source areas. (**c**) Multidimensional scaling (MDS) plot of heavy mineral data from aeolian sand and three potential sources in the Otindag. The MDS plot indicates that the aeolian sand in the Otindag has the strongest correlation with the sediments from the upwind areas Solid lines mark the closest neighbors and the dashed lines are the second closest neighbors. Key: OD: Otindag aeolian sand, Y: Yinshan mountain, L: lake basin, G: upwind sediments. (Sink areas: Otindag aeolian sand; source areas: Y, G, and L).

4.3. Dynamic Process of Provenance Supply in Potential Provenance Areas

Most sand seas in the world occur in basins and low-lying areas. These sand seas are formed by the weathering and denudation of surrounding mountain bedrock, as well as the transportation of large amounts of detrital materials under the action of gravity, fluvial, and aeolian processes. After deposition in the sand sea, these materials are further eroded, transported, and accumulated by wind action, eventually forming aeolian sand. The ZTR index of most aeolian sand samples in the Otindag is less than 10, indicating that the sand is primarily sourced from proximal source materials.

The upwind area is located northwest of the Otindag. The wind transport capacity is mainly governed by the threshold wind velocity and the duration of the wind velocity exceeding the threshold velocity [35]. By analyzing the spatial pattern of annual sand transport potential in the Otindag, the predominant sand transport directions were found from the west and northwest. The sand transport potential is higher in the northwest compared to the southeast, indicating a high wind energy environment. These favorable wind regimes promote the formation of aeolian sand in the dune field [54]. Moreover, the semi-fixed dune chain in the western part of Otindag moves towards the southeast at an average speed of 4.06 m/year. Similarly, the dune area in the northern part of the Otindag decreases and moves southeastward at a medium speed of 5.44 m/year [55]. Additionally, the ZTR value of aeolian sand increases from northwest to southeast, further confirming

the northwest-to-southeast direction of material transport. These findings align with the quantitative analysis of aeolian sand in the Otindag, which also indicates that the primary source of materials in the Otindag is the upwind area, contributing approximately 59 ± 14% of the aeolian sand (Figure 4). Overall, the prevailing west and northwest winds, combined with the extensive exposure of Tertiary red/blue-grey fluvial and lacustrine sediments, as well as Gobi sediments in the upwind area, along with the favorable topographic conditions of low in the northwest and high in the southeast, provide unique and optimal conditions for the formation of the Otindag in the downwind direction. Therefore, the upwind area serves as a significant supplier of aeolian sand to the Otindag.

The Yinshan Mountains lie in the southern region of the Otindag dune field, and a significant of loose sediments can be found at the northern foothills. Rivers flowing through the Yinshan Mountains play a crucial role in transporting these loose sediments to the southern edge of the Otindag. After transportation by the rivers, these sediments are further transported by wind, ultimately forming aeolian sand in the Otindag. According to Williams [56], areas surrounding riverbeds generally offer abundant sediments for the formation of dunes in desert environments. The upper reaches of the Luan River, located on the southern edge of the dune field, transport materials from the Yinshan Mountains to the southern edge of the Otindag. During dry and cold periods, the riverbed becomes exposed, during which the loose sediments are transported to the dune field through wind action. Moreover, during the flood season (June–September), alluvial deposits from the Yinshan Mountains can enter the river and be carried to the southern part of the dune field through short-term surface runoff. Material supply from the Yinshan Mountains in the southern part of the Otindag is primarily facilitated by the river system. However, in the arid area, the river system is controlled by seasonal precipitation, resulting in limited sediment supply. Furthermore, runoff from the upper reaches of the Luanhe River and other rivers in the Yinshan Mountains mainly affects the southern part of the Otindag. In recent years, the sediment content in the upper reaches of the Luanhe River has decreased due to sand source treatment projects [57]. Consequently, sediments transported by the Luanhe River and south-side runoff from the Yinshan Mountains contribute only 17 ± 10% of the sediments entering the Otindag (Figure 4).

With numerous large and small lakes, the Otindag has a distinctive landscape characterized by staggered lakes and sand dunes. Previous studies have reported on the occurrence of lake sediments in all deserts in northern China, indicating a long-standing coexistence of lakes and dunes in these regions [58]. This view has been confirmed in specific deserts in China, such as the Mu Us dune field and the Ulan Buh Desert [14,59]. During the Last Glacial Maximum, the Otindag experienced a dry and cold climate with intense winter monsoons. Under this condition, the water levels of rivers and lakes in the dune field significantly decreased, exposing extensive areas of lacustrine sedimentary sand layers. These exposed sediments provided abundant clastic materials and sand for aeolian sand movement [60,61]. The arid climate not only leads to rapid shrinkage of lakes but also hinders vegetation growth, resulting in prolonged exposure of loose lake sediments on the surface, eventually leading to the formation of sand dunes. During field investigations, numerous exposed lake basins and a small amount of lake sediments underlying basalt were discovered in the dune field, with surrounding sand dunes. This finding aligns with the research conclusion. The top basalt layer acts as a protective layer for the ancient lacustrine sediments, increasing their resistance to wind erosion. Therefore, the contribution of lacustrine sediments to the dune field is limited, accounting for only 23 ± 12% (Figure 4).

4.4. Provenance Implications for the Environment

Sandstorms are weather phenomena characterized by strong winds that lift and carry large amounts of sand and dust, leading to a significant decrease in air visibility [62,63]. These events are typically associated with arid climates and desertification, serving as a key indicator of the ecological conditions in northern China. The persistent occurrence of sandstorms in the Beijing-Tianjin region has had a detrimental impact on the region's ability

to achieve sustainable economic and social development. The Chinese government has prioritized addressing the issue of sandstorms and initiated the Beijing-Tianjin sandstorm source control phase I (2001–2005) and phase II (2006–2010) projects in 2001, which yielded positive outcomes [64]. As the main governance area, significant progress has been made in controlling sandstorms in the central, eastern, and southern Otindag. However, land degradation still exists in the western and northwestern parts of the Otindag [65]. Ping [66] noted that dust in the Otindag is mainly generated at the northwest edge rather than in the hinterland. Chang [67] suggested that wind-blown sand from the northwest region accumulates in the eastern region after dust storms. Our findings indicate that upwind serves as an immediate material source for the Otindag, accounting for 59%. Yinshan transports weathered products to the southern edge of the Otindag through rivers and then was transformed by wind and deposited mainly in the southern part of the Otindag, accounting for 17%. Lake sediments carried to sand by strong winds contributed 23% (Figure 8). Our research highlights the importance of enhancing land management strategies in the upwind regions of dust-affected areas to reduce the adverse effects of dust storms in the future. As the main source of sand for Beijing, the Otindag should implement differentiated management strategies for its comprehensive governance. In the eastern part of the Otindag, measures such as returning farmland to forest are primarily adopted; in the western and northern parts of the Otindag, a combination of measures including rotational grazing and grazing bans is used to increase the coverage of shrubs and grasses, reduce the hazards of desertification, and implement engineering measures for sand fixation; in the southern edge of the sandy land, an ecological protection system is established, mainly focusing on shrubs.

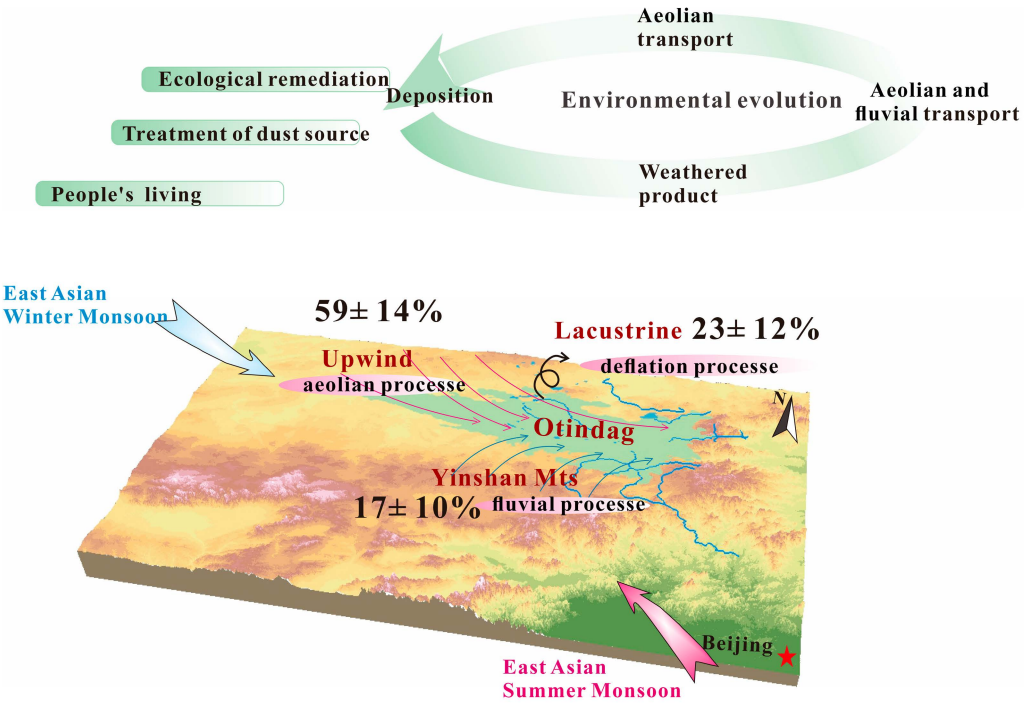

Figure 8. Schematic diagram of sediment transport processes from source areas to the Otindag and the provenance implications for the environment.

5. Conclusions

In this study, heavy mineral analysis was employed to compare aeolian sand sediments in the Otindag with samples from immediate potential source areas. The objective was to gain a comprehensive understanding of the sources of aeolian sand in the Otindag. The Conservativeness Index (CI), Consensus Ranking (CR), Consistent Tracer

Selection (CTS) methods and the FingerPro model were used to select the optimal set of tracers and quantify the contribution of each source to the aeolian sand samples.

Examination of sediment provenance evidence revealed the Otindag dune field to be the result of sedimentation from three distinct source areas: the upwind area of the sand plains (59 ± 14%), Yinshan Mountain (17 ± 10%), and the lake basin (23 ± 12%). The proposed sediment transport model elucidates that the upwind area primarily transports sediments to the entire Otindag through northwest winds. Rivers in the Yinshan Mountains transport sediments from the northern foot to the southern edge of the Otindag. Subsequently, influenced by wind, the lower layer is mainly deposited in the southern part of the dune field. Lacustrine sediments, widely distributed in the Otindag, significantly contribute to its overall composition.

In conclusion, this study enhances our understanding of the provenance and transport mechanisms of aeolian sand in the Otindag, providing valuable insights into ecological restoration policies to combat ecological degradation and land desertification in drylands.

Supplementary Materials: The following supporting information can be downloaded at: https://www.mdpi.com/article/10.3390/land13081194/s1, Table S1: Percentages of heavy minerals and key ratios within the Otindag; Table S2: Percentages of heavy minerals and key ratios within the Otindag; Figure S1: Ternary diagram of each tracer (taking sample OD-1 as an example). CR and CI values are represented by red and green numbers, respectively. Higher CR and CI values indicate higher consensus and conservative behavior. The blue points in the triangle rep-resent the individual solution of the single tracer model. G: upwind sediments, L: lake sediments, Y: Yinshan sediments. Sps: spessartite, Zo: zoisite, Gt: goethite, Ep: epidote, Bt: biotite, Ap: apatite, ΔtHM: Counting-△tHM, Rt: rutile, Chl: chlorite, SRD: Counting- SRD, Prp: pyrope, Tur: tourmaline, Ilm: ilmenite, Tr: tremolite, Mnz: magnetite, Opx: orthopy-roxene, Zr: zircon, Spn: sphene, Spl: spinel, tHM: Counting-tHM, Aln: allanite, Adr: an-dradite, Alm: almandine, Hbl: hornblende, Mag: magnetite, Fa: fayalite, Cpx: Clinopyrox-ene, Act: actinolite.

Author Contributions: Conceptualization, Y.Z. and Y.C.; methodology, Y.C.; software, I.L. and Y.C.; validation, I.L., Y.Z., A.L., P.L. and Z.D.; investigation, J.Z. and T.F.; writing—original draft, Y.C.; writing—review and editing, Y.Z. and I.L. All authors have read and agreed to the published version of the manuscript.

Funding: The contribution of Yali Zhou was supported by the National Natural Science Foundation of China, (No. 42071112). The contribution of Zhibao Dong was supported by the Science & Technology Fundamental Resources Investigation Program (Grant no. 2022FY202302; 2022FY202304).The contribution of Aimin Liang was supported by the National Natural Science Foundation of China (No. 42301004). The contribution of Ivan Lizaga was supported by the Research Foundation-Flanders (FWO, mandate 12V8622N).

Data Availability Statement: The raw data supporting the conclusions of this article will be made available by the authors upon request.

Conflicts of Interest: The authors declare no conflicts of interest.

References

1. Hara, Y.; Uno, I.; Wang, Z.F. Long-term variation of Asian dust and related climate factors. *Atmos. Environ.* **2006**, *40*, 6730–6740. [CrossRef]
2. Muhs, D.R. Evaluation of simple geochemical indicators of aeolian sand provenance: Late Quaternary dune fields of North America revisited. *Quat. Sci. Rev.* **2017**, *171*, 260–296. [CrossRef]
3. Maher, B.A.; Prospero, J.M.; Mackie, D.; Gaiero, D.; Hesse, P.P.; Balkanski, Y. Global connections between aeolian dust, climate and ocean biogeochemistry at the present day and at the last glacial maximum. *Earth Sci. Rev.* **2010**, *99*, 61–97. [CrossRef]
4. Sun, Y.B.; Yan, Y.; Nie, J.S.; Li, G.J.; Shi, Z.G.; Qiang, X.K.; Chang, H.; An, Z.S. Source-to-sink fluctuations of Asian aeolian deposits since the late Oligocene. *Earth Sci. Rev.* **2020**, *200*, 102963. [CrossRef]
5. Reynolds, J.F.; Smith, D.M.S.; Lambin, E.F.; Turner, B.L.; Mortimore, M.; Batterbury, S.P.; Walker, B. Global desertification: Building a science for dryland development. *Science* **2007**, *316*, 847–851. [CrossRef] [PubMed]
6. Garzanti, E.; Dinis, P.; Vermeesch, P.; Andò, S.; Hahn, A.; Huvi, J.; Limonta, M.; Padoan, M.; Resentini, A.; Rittner, M.; et al. Sedimentary processes controlling ultralong cells of littoral transport: Placer formation and termination of the Orange sand highway in southern Angola. *Sedimentology* **2018**, *65*, 431–460. [CrossRef]

7. Liang, A.M.; Dong, Z.B.; Su, Z.Z.; Qu, J.J.; Zhang, Z.C.; Qian, G.Q.; Wu, B.; Gao, J.L.; Yang, Z.L.; Zhang, C.X. Provenance and transport process for interdune sands in the Kumtagh Sand Sea, Northwest China. *Geomorphology* **2020**, *367*, 107310. [CrossRef]
8. Liu, Z.T.; Yang X, P. Geochemical-geomorphological evidence for the provenance of Aeolian sands and sedimentary environments in the Hunshandake Sandy Land, Eastern Inner Mongolia, China. *Acta Geol. Sin.-Engl.* **2013**, *87*, 871–884. [CrossRef]
9. Xie, J.; Ding, Z.L. Compositions of heavy minerals in Northeastern China sandlands and provenance analysis. *Sci. China Ser. D* **2007**, *50*, 1715–1723. [CrossRef]
10. Vermeesch, P.; Fenton, C.R.; Kober, F.; Wiggs, G.F.S.; Bristow, C.S.; Xu, S. Sand residence times of one million years in the Namib Sand Sea from cosmogenic nuclides. *Nat. Geosci.* **2010**, *3*, 862–865. [CrossRef]
11. Chang, Q.; Mishima, T.; Yabuki, S.; Takahashi, Y.; Shimizu, H. Sr and Nd isotope ratios and REE abundances of moraines in the mountain areas surrounding the Taklimakan Desert, NW China. *Geochem. J.* **2000**, *34*, 407–427. [CrossRef]
12. Lu, G.; Chen, X.W.; Zou, H.; Preto, N.; Huang, X.T.; Wang, C.C.; Shi, Z.Q.; Jin, X. Provenance of the first terrigenous sediments in the western Sichuan Basin during the Late Triassic: Implications for basin evolution from marine to continental. *Mar. Pet. Geol.* **2023**, *147*, 105992. [CrossRef]
13. Stevens, T.; Palk, C.; Carter, A.; Lu, H.; Clift, P.D. Assessing the provenance of loess and desert sediments in northern China using U-Pb dating and morphology of detrital zircons. *Bulletin* **2010**, *122*, 1331–1344. [CrossRef]
14. Zhang, C.; Li, Z.L.; Chen, Q.J.; Dong, S.P.; Yu, X.Y.; Yu, Q. Provenance of eolian sands in the Ulan Buh Desert, northwestern China, revealed by heavy mineral assemblages. *Catena* **2020**, *193*, 104624. [CrossRef]
15. Morton, A.; Knox, R.; Frei, D. Heavy mineral and zircon age constraints on provenance of the Sherwood Sandstone Group (Triassic) in the eastern Wessex Basin, UK. *Proc. Geol. Assoc.* **2016**, *127*, 514–526. [CrossRef]
16. Morton, A.C.; Hallsworth, C. Identifying provenance-specific features of detrital heavy mineral assemblages in sandstones. *Sediment. Geol.* **1994**, *90*, 241–256. [CrossRef]
17. Andò, S.; Garzanti, E.; Padoan, M.; Limonta, M. Corrosion of heavy minerals during weathering and diagenesis: A catalog for optical analysis. *Sediment. Geol.* **2012**, *280*, 165–178. [CrossRef]
18. Huber, B.; Bahlburg, H.; Pfänder, J.A. Single grain heavy mineral provenance of garnet and amphibole in the Surveyor fan and precursor sediments on the Gulf of Alaska abyssal plain Implications for climate-tectonic interactions in the St. Elias orogen. *Sediment. Geol.* **2018**, *372*, 173192. [CrossRef]
19. Morton, A.C.; Hallsworth, C.R.; Bahlburg, H.; Floyd, P.A. Processes controlling the composition of heavy mineral assemblages in sandstones. *Sediment. Geol.* **1999**, *124*, 3–30. [CrossRef]
20. Klages, M.G.; Hsieh, Y.P. Suspended Solids Carried by the Gallatin River of Southwestern Montana: II. Using Mineralogy for Inferring Sources. *J. Environ. Qual.* **1975**, *4*, 68–73. [CrossRef]
21. Walling, D.E.; Peart, M.R.; Oldfield, F.; Thompson, R. Suspended sediment sources identified by magnetic measurements. *Nature* **1979**, *281*, 281110a0. [CrossRef]
22. Walling, D.W.; Woodward, J.C.; Nicholas, A.P. A multi-parameter approach to fingerprinting suspended-sediment sources. In *Tracers in Hydrology. Proceedings of the International Symposium*; International Association of Hydrological Sciences: Yokohama, Japan; International Association of Hydrological Sciences: Oxfordshire, UK, 1993; pp. 329–338.
23. Zhang, X.C.; Liu, B. Using multiple composite fingerprints to quantify fine sediment source contributions: A new direction. *Geoderma* **2016**, *268*, 108–118. [CrossRef]
24. Palaz'on, L.; Gaspar, L.; Latorre, B.; Blake, W.H.; Navas, A. Identifying sediment sources by applying a fingerprinting mixing model in a Pyrenean drainage catchment. *J. Soils Sediments* **2015**, *15*, 2067–2085. [CrossRef]
25. Schuller, P.; Walling, D.E.; Iroumé, A.; Quilodrán, C.; Castillo, A.; Navas, A. Using 137Cs and 210Pbex and other sediment source fingerprints to document suspended sediment sources in small forested catchments in south-central Chile. *J. Environ. Radioact.* **2013**, *124*, 147–159. [CrossRef] [PubMed]
26. Laceby, J.P.; Gellis, A.C.; Koiter, A.J.; Blake, W.H.; Evrard, O. Preface—Evaluating the response of critical zone processes to human impacts with sediment source fingerprinting. *J. Soils Sediments* **2019**, *19*, 3245–3254. [CrossRef]
27. McCarthy, D.T.; Jovanovic, D.; Lintern, A.; Teakle, I.; Barnes, M.; Deletic, A.; Coleman, R.; Rooney, G.; Prosser, T.; Coutts, S.; et al. Source tracking usingmicrobial community fingerprints: Method comparisonwith hydrodynamic modelling. *Water Res.* **2017**, *109*, 253–265. [CrossRef] [PubMed]
28. Evrard, O.; Laceby, J.P.; Ficetola, G.F.; Gielly, L.; Huon, S.; Lefèvre, I.; Onda, Y. Environmental DNA provides information on sediment sources: A study in catchments affected by Fukushima radioactive fallout. *Sci. Total. Environ.* **2019**, *665*, 873–881. [CrossRef]
29. Gholami, H.; Telfer, M.; Blake, W.; Fathabadi, A. Aeolian sediment fingerprinting using a Bayesian mixing model. *Earth Surf. Proc. Land.* **2017**, *42*, 2365–2376. [CrossRef]
30. Song, Y.G.; Chen, X.L.; Li, Y.; Fan, Y.; Collins, A.L. Quantifying the provenance of dune sediments in the Taklimakan Desert using machine learning, multidimensional scaling and sediment source fingeprinting. *Catena* **2022**, *210*, 105902. [CrossRef]
31. Liang, A.M.; Zhang, Z.C.; Lizaga, I.; Dong, Z.B.; Zhang, Y.F.; Liu, X.K.; Xiao, F.J.; Gao, J.L. Which is the dominant source for the aeolian sand in the Badain Jaran Sand Sea, Northwest China: Fluvial or gobi sediments? *Catena* **2023**, *225*, 107011. [CrossRef]
32. Lizaga, I.; Latorre, B.; Gaspar, L.; Navas, A. Consensus ranking as a method to identify non-conservative and dissenting tracers in fingerprinting studies. *Sci. Total Environ.* **2020**, *720*, 137537. [CrossRef] [PubMed]
33. Latorre, B.; Lizaga, I.; Gaspar, L.; Navas, A. A novel method for analysing consistency and unravelling multiple solutions in sediment fingerprinting. *Sci. Total Environ.* **2021**, *789*, 147804. [CrossRef] [PubMed]

34. Liu, H.J.; Xu, Z.L.; Tang, C.; Jin, R.S.; Duan, M.; Wei, J.L.; Zeng, H.; Zhang, C. Provenance Characteristics of Uranium-bearing Sediments of the Upper Saihan Formation and Its Implications for Sandstone-type Uranium Mineralization in Manite Depression, Erlian Basin. *Earth Sci.* **2023**, 1–25, (In Chinese with English abstract). Available online: https://link.cnki.net/urlid/42.1874.P.20230511.1702.006 (accessed on 1 June 2017).
35. Fryberger, S.G.; Dean, G. Dune Forms and Wind Regime. In *A Study of Global Sand Seas*; McKee, E., Ed.; US Geological Survey Professional Paper 1052; IOP Publishing Ltd.: Washington, DC, USA, 1979; pp. 137–170. Available online: http://iopscience.iop.org/0034-4885/75/10/106901 (accessed on 1 June 2017).
36. Wang, Z.G.; Li, K.; Zhang, Z.C.; Tang, J.Z.; Chen, Y. Early Permian magmatism in northern Inner Mongolia, southeastern Central Asian Orogenic Belt: Implications on lithospheric extension in a post-collisional setting. *Lithos* **2022**, *426*, 106803. [CrossRef]
37. Liu, H.C.; Wang, J.C.; Lai, C.-K.; Li, Y.L.; Wang, J.F.; Song, C.Y.; Zhang, J.D.; Zhao, X.Z.; Qin, J.D. Anatomy of two Permian greenschist- to blueschist-facies tectonic mélanges in the Solonker Suture Zone (Inner Mongolia, northeastern China): Evidence for divergent double subduction and soft collision. *J. Geol. Soc.* **2020**, *177*, 981–996. [CrossRef]
38. Xiao, W.J.; Windley, B.F.; Hao, J.; Zhai, M.G. Accretion leading tocollision and the Permian Solonker suture, Inner Mongolia, China: Termination of the central Asian orogenic belt. *Tectonics* **2003**, *22*, 1069–1088. [CrossRef]
39. Tong, Y.; Hong, D.; Wang, T.; Shi, X.; Zhang, J.; Zeng, T. Spatial and Temporal Distribution of Granitoids in the Middle Segment of the Sino-Mongolian Border and Its Tectonic and Metallogenic Implications. *Acta Geosci. Sin.* **2010**, *31*, 395–412, (In Chinese with English abstract).
40. Song, S.G.; Wang, M.-M.; Xu, X.; Wang, C.; Niu, Y.L.; Allen, M.B.; Su, L. Ophiolites in the Xing'an-Inner Mongolia accretionary belt of the CAOB: Implications for two cycles of seafloor spreading and accretionary orogenic events. *Tectonics* **2015**, *34*, 2221–2248. [CrossRef]
41. Fossum, K.; Morton, A.C.; Dypvik, H.; Hudson, W.E. Integrated heavy mineral study of Jurassic to Paleogene sandstones in the Mandawa Basin, Tanzania: Sediment provenance and source-to-sink relations. *J. Afr. Earth Sci.* **2019**, *150*, 546–565. [CrossRef]
42. Nie, J.S.; Peng, W.B. Automated SEM EDS heavy mineral analysis reveals no provenance shift between glacial loess and interglacial paleosol on the Chinese Loess Plateau. *Aeolian Res.* **2014**, *13*, 71–75. [CrossRef]
43. Nie, J.; Peng, W.; Pfaff, K.; Möller, A.; Garzanti, E.; Andò, S.; Stevens, T.; Bird, A.; Chang, H.; Song, Y.; et al. Controlling factors on heavy mineral assemblages in Chinese loess and Red Clay. *Palaeogeogr. Palaeoclimatol. Palaeoecol.* **2013**, *381–382*, 110–118. [CrossRef]
44. Zhang, H.Z.; Lu, H.Y.; Zhou, Y.L.; Cui, Y.Y.; He, J.; Lv, H.Z.; Wang, K.X.; Wang, X.Y. Heavy mineral assemblages and U-Pb detrital zircon geochronology of sediments from the Weihe and Sanmen Basins: New insights into the Pliocene-Pleistocene evolution of the Yellow River. *Palaeogeogr. Palaeoclim. Palaeoecol.* **2020**, *562*, 110072. [CrossRef]
45. Garzanti, E.; Andò, S. Heavy mineral concentration in modern sands: Implications for provenance interpretation. *Dev. Sedimentol.* **2007**, *58*, 517–545. [CrossRef]
46. Hubert, J.F. A zircon-tourmaline-rutile maturity index and the interdependence of the composition of heavy mineral assemblages with the gross composition and texture of sandstones. *J. Sediment. Res.* **1962**, *32*, 440–450. [CrossRef]
47. Lizaga, I.; Latorre, B.; Bodé, S.; Gaspar, L.; Boeckx, P.; Navas, A. Combining isotopic and elemental tracers for enhanced sediment source partitioning in complex catchments. *J. Hydrol.* **2024**, *631*, 130768. [CrossRef]
48. Lizaga, I.; Latorre, B.; Gaspar, L.; Navas, A. *FingerPro: An R Packae for Sediment Source Tracing*; Zenodo: Geneva, Switzerland, 2018. [CrossRef]
49. Lizaga, I.; Latorre, B.; Gaspar, L.; Navas, A. FingerPro: An R Package for Tracking the Provenance of Sediment. *Water Resour. Manag.* **2020**, *34*, 3879–3894. [CrossRef]
50. Vermeesch, P.; Resentini, A.; Garzanti, E. An R package for statistical provenance analysis. *Sediment. Geol.* **2016**, *336*, 14–25. [CrossRef]
51. Pettijohn, F.J. *Sedimentary Rocks*; Harper & Row Publish: New York, NY, USA, 1975; pp. 1–523.
52. Zhang, X.J.; Pease, V.; Omma, J.; Benedictus, A. Provenance of Late Carboniferous to Jurassic sandstones for southern Taimyr, Arctic Russia: A comparison of heavy mineral analysis by optical and QEMSCAN methods. *Sediment. Geol.* **2015**, *329*, 166–176. [CrossRef]
53. Zhang, J.R.; Wei, C.J.; Chu, H. New model for the tectonic evolution of Xing' an -Inner Mongolia Orogenic Belt: Evidence from four different phases of metamorphism in Central Inner Mongolia. *Acta Petrol. Sin.* **2018**, *34*, 2857–2871, (In Chinese with English abstract).
54. Yang, X.; Zhu, B.; Wang, X.; Li, C.; Zhou, Z.; Chen, J.; Wang, X.; Yin, J.; Lu, Y. Late Quaternary environmental changes and organic carbon density in the Onqin Daga Dune field, eastern Inner Mongolia, China. *Glob. Planet. Change* **2008**, *61*, 70–78. [CrossRef]
55. Long, Q.X. *Study on Morphological Changes of Dune Inotindag Dune Field*; Shaanxi Normal University: Xi'an, China, 2018; (In Chinese with English abstract).
56. Williams, M. *Climate Change in Deserts: Past, Present and Future*; Cambridge University Press: Cambridge, UK, 2014. [CrossRef]
57. Li, Y.; Huang, S. Effects of landscape pattern change on flow and sediment processes in the Luanhe River Basin. *Acta Ecol. Sin.* **2017**, *37*, 2463–2485, (In Chinese with English abstract). [CrossRef]
58. Yang, X.P.; Li, H.W.; Conacher, A. Large-scale controls on the development of sand seas in northern China. *Quat. Int.* **2012**, *250*, 74–83. [CrossRef]
59. Liu, Q.Q.; Yang, X.P. Geochemical composition and provenance of aeolian sands in the Ordos Deserts, northern China. *Geomorphology* **2018**, *318*, 354–374. [CrossRef]
60. Yang, X.P.; Scuderi, L.; Paillou, P.; Liu, Z.T.; Li, H.W.; Ren, X. Quaternary environmental changes in the drylands of China A critical review. *Quat. Sci. Rev.* **2011**, *30*, 3219–3233. [CrossRef]
61. Yang, X.; Scuderi, L.A.; Wang, X.; Scuderi, L.J.; Zhang, D.; Li, H.; Forman, S.; Xu, Q.; Wang, R.; Huang, W.; et al. Groundwater sapping as the cause of irreversible desertification of Onqin Daga Dune fields, Inner Mongolia, northern China. *Proc. Natl. Acad. Sci. USA* **2015**, *112*, 702–706. [CrossRef] [PubMed]

62. Chen, S.; Liu, J.; Wang, X.; Zhao, S.; Chen, J.; Qiang, M.; Liu, B.; Xu, Q.; Xia, D.; Chen, F. Holocene dust storm variations over northern China: Transition from a natural forcing to an anthropogenic forcing. *J. Sci. Bull.* **2021**, *66*, 2516–2527. [CrossRef] [PubMed]
63. Issanova, G.; Kaldybayev, A.; Ge, Y.; Abuduwaili, J.; Ma, L. Spatial and Temporal Characteristics of Dust Storms and Aeolian Processes in the Southern Balkash Deserts in Kazakhstan, Central Asia. *Land* **2023**, *12*, 668. [CrossRef]
64. Yang, H.; Zhao, S.; Qin, Z.; Qi, Z.; Jiao, X.; Li, Z. Differentiation of Carbon Sink Enhancement Potential in the Beijing–Tianjin–Hebei Region of China. *Land* **2024**, *13*, 375. [CrossRef]
65. Liu, X.; Li, L.; Qin, F.C.; Li, Y.H.; Chen, J.X.; Fang, X.N. Ecological policies enhanced ecosystem services in the Hunshandak sandy land of China. *Ecol. Indic.* **2022**, *144*, 109450. [CrossRef]
66. Ping, Y.; Liu, X.J.; Yang, Q.G. Analysis on dust emission characteristics in the western desertificational fringe area of Hunshandake Sand-Land. In Proceedings of the 2009 International Conference on Environmental Science and Information Application Technology, Wuhan, China, 4–5 July 2009; IEEE: Piscataway, NJ, USA, 2009; Volume 3, pp. 617–620. [CrossRef]
67. Chang, X.T.; Guo, J.Y.; Wang, X.P. Detecting the amount of eroded and deposited sand using DInSAR. *TAO* **2011**, *22*, 187–194. [CrossRef]